Revision 1

The $NaCl–CaCO_3$ and $NaCl–MgCO_3$ systems at 6 GPa: Link between saline and carbonatitic diamond forming melts

Anton Shatskiy[1,2,3*], Ivan V. Podborodnikov[1,2], Anastasia S. Fedoraeva[1,2], Anton V. Arefiev[1,2,3], Altyna Bekhtenova[1,2], and Konstantin D. Litasov[3]

[1]Sobolev Institute of Geology and Mineralogy Siberian Branch Russian Academy of Science, Novosibirsk 630090, Russia

[2]Novosibirsk State University, Novosibirsk 630090, Russia

[3]Vereshchagin Institute for High Pressure Physics, Russian Academy of Science, Troitsk, Moscow, 108840, Russia

*telephone: +7 (913)-385-61-29, e-mail: shatskiyantonf@gmail.com

Keywords: chloride-carbonate, saline HDF, carbonatitic HDF, *T-X* diagram, Earth's mantle.

Abstract

The frequent occurrence of chlorides and carbonates in the form of microinclusions of melts or high-density fluid (HDF) in diamonds and igneous minerals of kimberlites worldwide generates genuine interest in their phase diagrams under pressure. Here, we present the first experimental results on the phase relations in the $NaCl–CaCO_3$ and $NaCl–MgCO_3$ systems at 6 GPa in the range 1000-1600 °C performed using multianvil press. We found that both systems have the eutectic type of phase diagrams. The subsolidus assemblages are represented by halite + aragonite and halite + magnesite. Halite-aragonite eutectic is situated just below 1200 °C and has a composition of 40 wt% NaCl and 60 wt% $CaCO_3$. Halite-magnesite eutectic is located at 1300 °C and has a

composition of 72 wt% NaCl and 28 wt% $MgCO_3$. Halite melting point was established at 1500 °C. Complete miscibility between carbonate and chloride liquids was observed up to 1600 °C. The obtained results support the hypotheses that saline HDF is either a low-temperature derivative or precursor of mantle carbonatite HDF. The data obtained also do not exclude an alternative hypothesis, according to which saline HDF are formed as a result of the reduction of the carbonate component of chloride-containing carbonatite melts to diamond.

Introduction

Alkaline chlorides and carbonates are important constituents of diamond-forming HDFs (Navon et al. 1988; Izraeli et al. 2001; Kaminsky et al. 2013; Jablon and Navon 2016; Zedgenizov et al. 2018) and a liquid component of kimberlite magma carrying diamonds to the surface (Kamenetsky et al. 2004; Kamenetsky et al. 2014; Abersteiner et al. 2019; Golovin et al. 2020; Sharygin et al. 2021). Although a natural abundance of Cl in the mantle does not exceed 30 wt ppm (Palme and O'Neill 2003; Shimizu et al. 2016), the probes of deep-seated magmas (basalt, komatiite, kimberlite), entrapped as inclusions in mantle minerals, indicate an excess of chlorine, implying the abundance of chlorine in the source regions of these magmas (Kamenetsky et al. 2009; Hanyu et al. 2019; Asafov et al. 2020). Subducted seawater-altered and carbonated oceanic crust is considered a likely source of chlorine (Weiss et al. 2015; Hanyu et al. 2019; Asafov et al. 2020). Kendrick et al. (2011) found that a significant portion of chlorine survives deserpenization at subarc depth and therefore can be subducted to depths greater than 70 km.

Inclusions in diamonds are the deepest probes of mantle melts and HDFs extending to the lower mantle (Kaminsky et al. 2013; Kaminsky et al. 2016). Their composition varies between a silicic melt, rich in Si, K, Al, water, and a minor carbonate; carbonatitic, rich in carbonate, Ca, Mg, K, and a saline, rich in Cl, K, Na, water; and carbonates (Bulanova et al. 1988; Navon et al. 1988; Schrauder and Navon 1994; Izraeli et al. 2001; Klein-BenDavid et al. 2009; Zedgenizov et al. 2009; Zedgenizov et al. 2011; Jablon and Navon 2016; Shatsky et al. 2019). Continuous

variations in the composition of HDFs suggest a genetic link between the endmembers (Klein-BenDavid et al. 2007; Weiss et al. 2015).

Experiments show that silicic and carbonatitic melts are immiscible and can be derived by partial melting of recycled hydrothermally altered basalts (Kiseeva et al. 2012) or carbonated pelites at a depth of about 200 km (Shatskiy et al. 2019). The carbonate melt dissolves chlorides and remains in equilibrium with silicate minerals up to 1380-1450 °C at 4.5-5.5 GPa. At higher temperatures, either an immiscible carbonate-silicate melt appears in addition to chloride-carbonate melt (Safonov et al. 2007; Litasov and Ohtani 2009; Safonov et al. 2009a; Safonov et al. 2009b; Safonov et al. 2011) or carbonatite melt evolves toward silicate melt at 1500-1700 °C (Litasov et al. 2010; Safonov et al. 2011).

However, a genetic link between saline and carbonatitic endmembers remains controversial and experimentally unresolved. Some hypotheses consider the saline HDFs as either a slab-derived precursor of carbonatitic melts (Weiss et al. 2015) or a low-temperature derivative of mantle carbonatite melts (Shatskiy et al. 2019). On the other hand, immiscibility between molten chlorides and carbonates, if any, can be involved to explain their genetic link (Veksler 2004). Yet, phase equilibria in chloride-carbonate systems are still experimentally challenging.

Here, we studied solidus and melting phase relations in the binary NaCl–$CaCO_3$ and NaCl–$MgCO_3$ systems at 6 GPa in the range 1000-1600 °C and discussed the constrained *T-X* diagram with implication to the mantle saline and carbonatitic melts/HDFs.

Methods

Starting mixtures were prepared from reagent grade NaCl, $CaCO_3$, and natural magnesite (<0.1% impurity) from Brumado (Bahia, Brazil). Before weighing, NaCl and $CaCO_3$ were calcined at 500 °C and magnesite – at 300 °C. The powders were blended in an agate mortar with acetone. The prepared mixtures were dried at 300 °C in air and stored in a vacuum oven at 100 °C.

Experiments were run using a 1500-ton DIA-type press (Osugi et al. 1964) at IGM SB RAS. Eight 26-mm tungsten carbide cubes ("Fujilloy N-05") with 12-mm truncations were used as the inner-stage anvils. Pyrophyllite gaskets 4.0 mm in width and thickness were employed to support anvils flanks. Pressure medium (PM), made of semisintered ZrO_2 ceramics (OZ-8C, MinoYogyo Co., Ltd) (Shatskiy et al. 2011), was shaped as 20.5-mm octahedron with ground edges and corners. Graphite heater, 4.0 mm in inner diameter, 0.25-mm thick, and 11 mm height, was inserted diagonally at the center of PM. W97%Re3%-W25%Re25% thermocouple wire, 0.1 mm in diameter, were inserted in the heater center and electrically insulated by Al_2O_3 tubes. The powdered samples were loaded in graphite cassettes (multicharged samples holders), placed from both sides of the thermocouple (Shatskiy et al. 2022). ZrO_2 plugs, 2.2 mm in height, were inserted from both heater ends. Room- and high-temperature pressure calibrations were done using known phase transitions in Bi, Ba, SiO_2, and $CaGeO_3$ (Shatskiy et al. 2013b; Shatskiy et al. 2018). No correction of the pressure effect on thermocouple EMF was applied. Uncertainty in pressure and temperature estimates is estimated to be less than 0.5 GPa and 25 °C.

Prior to the experiment, the prepared high-pressure cells were stored in a vacuum oven at 200 °C for ≥ 12 h. The experiments were conducted by room-temperature compression to a press-load of 6.5 GPa during 4 h, heating to target temperature with a rate of 50 °C/min, maintaining the target temperature in the thermocouple control mode within 2-3 °C of target value at constant press load, quenching below 150 °C in a few seconds, followed by 5-h decompression.

Recovered graphite cassettes were cut using a low-speed diamond saw and mounted into epoxy. Samples were ground in using 400(37)-, 1000(13)-, and 1500(9)-mesh(μm) sandpapers and a 3-μm diamond past. WD-40 spray was employed as a lubricant. Before a carbon coating, the samples were stored in benzine.

Samples were studied using a MIRA 3 LMU scanning electron microscope (Tescan Orsay Holding, Brno-Kohoutovice, Czech Republic), coupled with an INCA energy-dispersive X-ray microanalysis system 450, equipped with the liquid nitrogen-free Large area EDX X-Max-80

Silicon Drift Detector (Oxford Instruments Nanoanalysis Ltd., High Wycombe, UK) at IGM SB RAS. It is generally accepted that unlike wavelength dispersive X-ray spectroscopy (WDS), energy dispersive X-ray spectroscopy (EDS) is a semi-quantitative method. But that is no longer true. The recent advances in EDS performance with the silicon drift detector (SDD) enable accuracy and precision equivalent to that of WDS in the case of routine analysis of rock-forming minerals (Lavrent'ev et al. 2015; Newbury and Ritchie 2015). We also need to emphasize that the accuracy of the WDS analysis decreases dramatically in the case of alkali carbonate samples (Arefiev et al. 2019).

Energy-dispersive X-ray spectra (EDX) were collected by using an electron beam-rastering method, in which the stage is stationary while the electron beam moves over the surface area, with dimensions 5–50 μm (for minerals) and 50–500 μm (for a quenched melt) at 20 kV accelerating voltage and 1.5 nA beam current. Live counting time for X-ray spectra was 20 s.

Results

After the experiments, the bulk ratio of sodium and chlorine in the recovered samples and the chloride-carbonate melt remained unchanged and approaches the initial value Na/Cl = 1 (Tables 1, 2, S1-S9). Thus, whole sodium belongs to chloride and chlorine does not form a separate fluid phase. The composition of the phases and the bulk composition of the systems, which will be discussed below, are expressed in terms of the sodium concentration as Na#2 = $Na_2CO_3/(Na_2CO_3+CaCO_3+MgCO_3)\cdot 100$ mol%.

The NaCl-$CaCO_3$ system

At 1000 (run D281, 98 h) and 1100 °C (runs D227, 37 h and D283, 48 h), the samples are represented by homogeneous aggregates of halite and aragonite. The latter was identified by Raman spectroscopy. Aragonite forms euhedral to subhedral isometric grains 5-40 μm in size. Halite fills the space between the aragonite crystals (Fig. 1a-c).

130 The first melt appears at 1200 °C (run D282, 24 h) (Tables 1, S3). At this temperature, the
131 sample with Na2# 36 consists of quenched melt, whereas one with Na2# 67 is represented by halite
132 crystals in the low-temperature (LT) side, and quenched melt in the high-temperature (HT) side
133 (Fig. 1d). Halite forms an aggregate of crystals up to 400 μm in size elongated in the direction of
134 the HT side (Fig. 1d). The coexisting chloride-carbonate melt contains 45 wt% NaCl (Na2# 41)
135 (Fig. 2).
136 At 1250 °C (runs D265, 3 h and D266, 7 h) and bulk Na2# 18, aragonite coexists with the
137 chloride-carbonate liquid, containing 36 wt% NaCl (Na2# 33). As bulk Na2# increases from 82 to
138 95, the fraction of solid phase, halite, increases (Fig. 1e, g), while the liquid composition remains
139 constant, 63-64 wt% NaCl (Na2# 59-61) (Fig. 2, Tables 1, S4). The melt quenches in a dendritic
140 aggregate of halite and aragonite crystals (Fig. 1f).
141 As temperature increases to 1300 (run D284, 3 h) and 1400 °C (run D263, 2 h), the NaCl
142 content in the melt, coexisting with halite, increases to 71 wt% (Na2# 68) and 93 wt% (Na2# 91),
143 respectively (Fig. 2, Tables S5, S6).
144 At 1300 °C (run D216, 4 h) / bulk Na2# 33, 1400 °C (run D263, 2 h) / bulk Na2# 40, 1500
145 °C (runs D287, 1 h, D223, 6 h) / bulk Na2# 6, 46, 82, and 1600 °C (run D224, 3 h) / bulk Na2# 32
146 and 82, the samples are completely molten (Fig. 2, Tables 1, S5-S8).
147 Halite melting experiment was conducted at 1500 °C (run D287, 1 h). A piece of Pt (cylinder)
148 was used as a marker of melting. Unfortunately, it stuck to the wall and therefore did not sink (Fig.
149 1h). However, in this run, the HT sample side consists of a dendritic aggregate of NaCl (former
150 liquid), whereas balk halite crystals appear on the LT side (Fig. 1h, i). The coexistence of both
151 solid and liquid NaCl indicates that 1500 °C corresponds to the halite melting point at 6 GPa. This
152 is consistent with the previous experimental data at 6 GPa: 1500 °C (extrapolated from 3.9 GPa
153 (Pistorius 1966), 1504 (uncorrected) and 1527 °C (corrected) (Akella and Kennedy 1969), and
154 results by Li and Li (2015) within experimental uncertainty.
155

The NaCl-$MgCO_3$ system

At 1000 (run D281, 98 h), 1100 (run D227, 37 h), 1200 (run D218, 18 h), and 1250 °C (runs D265, 3 h, D266, 7 h), the samples consist of a homogeneous aggregate of magnesite and halite crystals 5-100 μm in size (Fig. 3a-c, Tables 2, S1-S4).

The first melting occurs at 1300 °C (runs D216, 4 h, D284, 3 h). The melt appears as a thin, up to 40-100 μm, layer adjoin to the HT capsule end (Fig. 3d-e). A single-phase layer of magnesite or halite appears at the interface with melt pool at bulk Na2# 18 and 46 (Fig. 3d, e) and Na2# 82 and 86 (Fig. 3f), respectively. The lower temperature sample side is represented by the subsolidus assemblage, magnesite + halite (Fig. 3d-f). The incipient melt has a uniform chloride-carbonate composition and contains 70-71 wt% NaCl (Na2# 63-65) (Table 2, S5).

As temperature increases to 1400 °C at bulk Na2# 46 (run D286, 2 h) and 1500 °C at bulk Na2# 33 (run D287, 1 h), the NaCl content in the chloride-carbonate melt decreases to 65 wt% (Na2# 58) and 52 wt% (Na2# 44), respectively (Fig. 3, Tables 2, S6, S7). The melt coexists with a dome-shaped aggregate of magnesite crystals adjoined to the LT side (Fig. 3g, i).

At 1400 °C and bulk Na2 = 97 (run D286, 2 h), the sample mainly consists of an aggregate of large (up to 500 μm) halite crystals and a thin layer of melt adjacent to the HT capsule end (Fig. 3h). The melt contains 83 wt% NaCl (Na2# 78) (Fig. 4, Table 2, S6)

At 1500 °C (run D223, 6 h) / bulk Na2 = 46, 82 and 1600 °C (run D224, 3 h)/ Na2 = 38, 79, the samples melt completely (Tables 2, S7, S8).

Mutual solubility of halite-aragonite and halite-magnesite does not exceed 0.4 wt%, which is within the uncertainty of measurements, of about 0.5 wt% (Tables 2, S1-S7).

The NaCl-$CaCO_3$ system undried

To clarify the impact of water on the phase relationships in the chloride-carbonate systems, an experiment with the undried NaCl-$CaCO_3$ mixtures was performed at 1100 °C (run D271, 5 h). The results of this run are illustrated in Fig. 5 and summarized in Fig. 6 and Table S9. Unlike dry

conditions, where the melting begins 100 °C higher, all undried samples exhibit melting. At bulk Na2# 18, the sample consists of aragonite crystals up to 300 μm in length, grown in the LT side, and chloride-carbonate melt containing 32 wt% NaCl (Na2# 29) (Fig. 5a, Table S9). The sample with Na2# 33 is completely molten (Table S9). At bulk Na2# 67 and 82, halite crystals up to 500 μm in size appear at the LT side, while the melt segregates at the HT side (Fig. 5b, c). The NaCl content in the melt coexisting with halite increases from 61 to 72 wt% (Na2# 58→69) as the bulk Na2# increases from 67 to 82 (Fig. 6, Table S9), which is indicative of the presence of additional component, water.

Discussion

At 6 GPa, the studied chloride-carbonate systems have eutectic *T-X* diagrams (Fig. 7a, c). The NaCl-$CaCO_3$ binary has the halite + aragonite subsolidus assemblage. This indicates that the free energy of NaCl + $CaCO_3$ is higher than that of Na_2CO_3 + $CaCl_2$, like that at 1 atm and temperatures ranging from room to 600 °C (Peh et al. 2017). The first melt was established at 1200 °C. At this temperature and bulk Na# 67, halite coexists with the melt with Na2# 41, while at bulk Na2# 36, complete melting was observed. Interpolation of the liquidus lines gives the eutectic at 1185 °C and Na# 36 (Fig. 2). The NaCl-$MgCO_3$ binary has the halite + magnesite subsolidus assemblage, which melts at 1300 °C (Fig. 4). Eutectic melts have a carbonate-chloride composition. In the NaCl-$CaCO_3$ system, the melt is more enriched in carbonate with 40 wt% NaCl and 60 wt% $CaCO_3$ (Fig. 7a). In the NaCl-$MgCO_3$ system, the melt is enriched in chloride with 72 wt% NaCl and 28 wt% $MgCO_3$ but appears 100 °C higher (Fig. 7c). Chloride and carbonate melts are completely miscible in the entire range of the studied compositions and temperatures up to 1600 °C (Figs. 2, 4).

Unlike the studied chloride-carbonate systems at 6 GPa, the corresponding carbonate systems Na_2CO_3–$CaCO_3$ (Shatskiy et al. 2013c) and Na_2CO_3–$MgCO_3$ (Shatskiy et al. 2013a) have intermediate compounds, represented by the following double carbonates: $Na_2Ca_4(CO_3)_5$-*P*6_3*mc*

208 (Rashchenko et al. 2017), and $Na_2Ca_3(CO_3)_4$-*P*1*n*1 (Gavryushkin et al. 2014), $Na_4Ca(CO_3)_3$-*Ia*3*d*
209 (Rashchenko et al. 2018), and $Na_2Mg(CO_3)_2$ eitelite (Fig. 7b, d). The above compounds melt
210 congruently, except for $Na_2Ca_4(CO_3)_5$, which decomposes below solidus (Fig. 7b). In this study,
211 we introduced Cl into the systems, in amounts equal to Na (i.e., mole ratio Na/Cl = 1) and found
212 no double carbonates. This indicates the preferred distribution of Na in halite, and Ca and Mg in
213 carbonates. Considering the above results, we proposed that the formation of double Na-Ca and
214 Na-Mg carbonates in the chloride-carbonate systems should occur at Na/Cl ratios > 1.

215 The Na-rich eutectics in the Na_2CO_3–$CaCO_3$ are situated just below 1200 °C similar to the
216 NaCl–$CaCO_3$, while the Ca-rich carbonate eutectic is 100 °C higher (Fig. 7a, b). The Na-rich
217 eutectic in the Na_2CO_3–$MgCO_3$ is located at 1200 °C, which is 100 °C lower than the NaCl–
218 $MgCO_3$ eutectic (Fig. 7c, d). Thus, replacing Na_2CO_3 with NaCl does not lead to a significant
219 change in the temperatures of the eutectics and all of them fall in the range 1200-1300 °C.
220 Nevertheless, the presence of intermediate phases melting congruently determines the presence of
221 temperature barriers, which prevents the formation of high-sodium carbonate melts. The absence
222 of such barriers in chloride-carbonate systems, as well as a sufficiently alkaline composition of
223 eutectics, especially NaCl–$MgCO_3$, suggests the possibility of the formation of highly alkaline
224 chloride-carbonate melts (Fig. 7a, c). The presence of water should contribute to this tendency,
225 shifting the composition of the chloride-carbonate melt to a more NaCl-rich and expanding its
226 stability to lower temperatures (Fig. 6).

227 According to the data obtained, the cooling of a carbonate melt, containing NaCl, should be
228 accompanied by fractional crystallization of Ca and/or Mg carbonates, changing the composition
229 of the melt toward chloride-carbonate. The solidification of this melt leads to the formation of Ca
230 and Mg carbonates and halite. Alkaline earth carbonates are poorly soluble in water and water
231 affects their melting points to a lesser extent than halite. Indeed, the experiment with undried
232 starting mixtures showed lower melting temperatures and a shift of melt composition toward NaCl
233 (Fig. 6).

234

235 **Implications**

236 Complete miscibility between carbonate and chloride liquids was established from melting
237 beginning to 1600 °C (Figs. 2, 4). Thus, the results obtained do not support the guess of the
238 formation of chloride and carbonate melts as a result of liquid immiscibility (Veksler 2004), at
239 least at mantle pressures. At the same time, the eutectic type of the established diagrams supports
240 the hypotheses of the low-temperature nature of water-rich chloride melt/HDF in which it is
241 considered either as precursors of carbonatite melt (Weiss et al. 2015) (Fig. 8b) or as its low-
242 temperature derivative (Shatskiy et al. 2019) (Fig. 8a).

243 The Earth is depleted in chlorine by factor 10 relative to chondritic and solar abundances
244 (Sharp and Draper 2013). The upper mantle is largely depleted in chlorine: the estimate of chlorine
245 abundances in the sub-continental mantle, based on data from African and Siberian coated
246 diamonds, is 3 ppm (Burgess et al. 2002). High-pressure Cl partitioning experiments between
247 molten metal and silicate indicate that the Cl content of the core is also negligible (Sharp and
248 Draper 2013). The similarity of mantle, crust, and carbonaceous chondrites establishes that there
249 was no Cl isotopic fractionation during differentiation of the Earth (Sharp et al. 2007). The lack of
250 chlorine was attributed to its loss during the giant moon-forming impact (Sharp and Draper 2013).
251 The oceans are considered the main concentrator of chlorine. Seawater and solute Cl^- incorporates
252 in hydrated serpentinite rocks within subducting oceanic lithosphere (Kendrick et al. 2011).
253 Significant portions of chlorine and carbonates survive deserpenization at subarc depths of about
254 70 km (Kerrick and Connolly 2001; Kendrick et al. 2011).

255 In the present study, we found that at a pressure of 6 GPa corresponding to a depth of 200
256 km, the NaCl-$CaCO_3$ and NaCl-$MgCO_3$ eutectics are situated at 1200-1300 °C, which is 200-300
257 °C higher than the hottest subduction geotherms. Thus, our high-pressure data indicate that halite
258 associated with aragonite or magnesite can survive subduction to a depth of 200 km. Warming of
259 oceanic slabs, diving beneath the continental lithospheric mantle by low-angle subduction, e.g.

(Currie and Beaumont 2011), should be accompanied by partial melting with the formation of a chloride-carbonate melt containing up to 20-40 wt% Cl (Tables S3-S9). The obtained experimental results are consistent with the presence of saline inclusions in fibrous and monocrystalline diamonds from kimberlites and placers worldwide derived from the base of ancient cratons (Izraeli et al. 2001; Jablon and Navon 2016).

Our preliminary experimental results have shown that the reduction of the NaCl-$CaCO_3$ and NaCl-$MgCO_3$ melts by iron metal at 6 GPa yields precipitation of carbon (solute in iron metal, iron carbides, metastable graphite or diamond) and ferropericlase/ magnesiowustite and shifts the melt composition toward higher NaCl (Fig. 4). Thus, the interaction of alkaline chloride-bearing carbonate melts formed in the subduction zones with the reduced mantle should be accompanied by the reduction of the carbonate component. This should be accompanied by diamond crystallization and shift the composition of the melt from carbonatitic to saline (Fig. 8c).

Thus, the continuous trend in the compositions from carbonatitic to saline HDFs entrapped as microinclusions in natural diamonds can be explained by (1) fractional crystallization of the Cl-bearing carbonatite melt; (2) melting of carbonated mantle domains induced by saline HDF; (3) reduction of Cl-bearing carbonatitic melt.

Nomenclature

Arg – aragonite, Cal-V – *R*-3*m* calcite V, Cal-Vb – $P2_1/m$ calcite Vb, Hl – halite, L – liquid, Mgs – magnesite, 'q-' – quench phase.

Acknowledgments

We are grateful to Valentina G. Butvina and the anonymous reviewer for constructive reviews and Fabrizio Nestola for editorial handling. This work is financially supported by Russian Science Foundation (project No 21-17-00024).

References

Abersteiner, A., Kamenetsky, V.S., Goemann, K., Giuliani, A., Howarth, G.H., Castillo-Oliver, M., Thompson, J., Kamenetsky, M., and Cherry, A. (2019) Composition and emplacement of the Benfontein kimberlite sill complex (Kimberley, South Africa): Textural, petrographic and melt inclusion constraints. Lithos, 324, 297-314.

Akella, J., and Kennedy, G.C. (1969) Melting of sodium cloride to 65 kbar. Physical Review, 185(3), 1135-1140.

Arefiev, A.V., Shatskiy, A., Podborodnikov, I.V., Behtenova, A., and Litasov, K.D. (2019) The system K_2CO_3–$CaCO_3$–$MgCO_3$ at 3 GPa: Implications for carbonatite melt compositions in the subcontinental lithospheric mantle. Minerals, 9(5), 296.

Asafov, E.V., Sobolev, A.V., Batanova, V.G., and Portnyagin, M.V. (2020) Chlorine in the Earth's mantle as an indicator of the global recycling of oceanic crust. Russian Geology and Geophysics, 61(9), 937-950.

Bulanova, G.P., Novgorodov, P.G., and Pavlova, L.A. (1988) The first find of a melt inclusion in diamond from the Mir pipe. Geokhimia, 756-765 (in Russian).

Burgess, R., Layzelle, E., Turner, G., and Harris, J.W. (2002) Constraints on the age and halogen composition of mantle fluids in Siberian coated diamonds. Earth and Planetary Science Letters, 197(3-4), 193-203.

Currie, C.A., and Beaumont, C. (2011) Are diamond-bearing Cretaceous kimberlites related to low-angle subduction beneath western North America? Earth and Planetary Science Letters, 303(1-2), 59-70.

Druzhbin, D., Rashchenko, S., Shatskiy, A., and Crichton, W. (Under review) New high-pressure, high-temperature $CaCO_3$ polymorph. ACS Earth and Space Chemistry.

Gavryushkin, P.N., Bakakin, V.V., Bolotina, N.B., Shatskiy, A.F., Seryotkin, Y.V., and Litasov, K.D. (2014) Synthesis and crystal structure of new carbonate $Ca_3Na_2(CO_3)_4$ homeotypic

with orthoborates $M_3Ln_2(BO_3)_4$ (M = Ca, Sr, and Ba). Crystal Growth & Design, 14(9), 4610-4616.

Golovin, A.V., Sharygin, I.S., Korsakov, A.V., Kamenetsky, V.S., and Abersteiner, A. (2020) Can primitive kimberlite melts be alkali-carbonate liquids: Composition of the melt snapshots preserved in deepest mantle xenoliths. Journal of Raman Spectroscopy, 51(9), 1849-1867.

Hanyu, T., Shimizu, K., Ushikubo, T., Kimura, J.-I., Chang, Q., Hamada, M., Ito, M., Iwamori, H., and Ishikawa, T. (2019) Tiny droplets of ocean island basalts unveil Earth's deep chlorine cycle. Nature communications, 10(1), 1-7.

Izraeli, E.S., Harris, J.W., and Navon, O. (2001) Brine inclusions in diamonds: a new upper mantle fluid. Earth and Planetary Science Letters, 187(3-4), 323-332.

Jablon, B.M., and Navon, O. (2016) Most diamonds were created equal. Earth and Planetary Science Letters, 443, 41-47.

Kamenetsky, M.B., Sobolev, A.V., Kamenetsky, V.S., Maas, R., Danyushevsky, L.V., Thomas, R., Pokhilenko, N.P., and Sobolev, N.V. (2004) Kimberlite melts rich in alkali chlorides and carbonates: A potent metasomatic agent in the mantle. Geology, 32(10), 845-848.

Kamenetsky, V.S., Kamenetsky, M.B., Weiss, Y., Navon, O., Nielsen, T.F.D., and Mernagh, T.P. (2009) How unique is the Udachnaya-East kimberlite? Comparison with kimberlites from the Slave Craton (Canada) and SW Greenland. Lithos, 112, 334-346.

Kamenetsky, V.S., Golovin, A.V., Maas, R., Giuliani, A., Kamenetsky, M.B., and Weiss, Y. (2014) Towards a new model for kimberlite petrogenesis: Evidence from unaltered kimberlites and mantle minerals. Earth-Science Reviews, 139, 145-167.

Kaminsky, F.V., Wirth, R., and Schreiber, A. (2013) Carbonatitic inclusions in deep mantle diamond from Juina, Brazil: new minerals in the carbonate-halide association. Canadian Mineralogist, 51(5), 669-688.

336 Kaminsky, F.V., Ryabchikov, I.D., and Wirth, R. (2016) A primary natrocarbonatitic association
337 in the Deep Earth. Mineralogy and Petrology, 110(2-3), 387-398.
338 Kendrick, M.A., Scambelluri, M., Honda, M., and Phillips, D. (2011) High abundances of noble
339 gas and chlorine delivered to the mantle by serpentinite subduction. Nature Geoscience,
340 4(11), 807-812.
341 Kerrick, D.M., and Connolly, J.A.D. (2001) Metamorphic devolatilization of subducted oceanic
342 metabasalts: implications for seismicity, arc magmatism and volatile recycling. Earth and
343 Planetary Science Letters, 189(1-2), 19-29.
344 Kiseeva, E.S., Yaxley, G.M., Hermann, J., Litasov, K.D., Rosenthal, A., and Kamenetsky, V.S.
345 (2012) An experimental study of carbonated eclogite at 3.5–5.5 GPa—implications for
346 silicate and carbonate metasomatism in the cratonic mantle. Journal of Petrology, 53(4),
347 727-759.
348 Klein-BenDavid, O., Izraeli, E.S., Hauri, E., and Navon, O. (2007) Fluid inclusions in diamonds
349 from the Diavik mine, Canada and the evolution of diamond-forming fluids. Geochimica
350 Et Cosmochimica Acta, 71(3), 723-744.
351 Klein-BenDavid, O., Logvinova, A.M., Schrauder, M., Spetius, Z.V., Weiss, Y., Hauri, E.H.,
352 Kaminsky, F.V., Sobolev, N.V., and Navon, O. (2009) High-Mg carbonatitic
353 microinclusions in some Yakutian diamonds - a new type of diamond-forming fluid.
354 Lithos, 112(S2), 648-659.
355 Lavrent'ev, Y.G., Karmanov, N.S., and Usova, L.V. (2015) Electron probe microanalysis of
356 minerals: Microanalyzer or scanning electron microscope? Russian Geology and
357 Geophysics, 56(8), 1154-1161.
358 Li, Z., and Li, J. (2015) Melting curve of NaCl to 20 GPa from electrical measurements of
359 capacitive current. American Mineralogist, 100(8-9), 1892-1898.

Litasov, K.D., and Ohtani, E. (2009) Phase relations in the peridotite–carbonate–chloride system at 7.0–16.5 GPa and the role of chlorides in the origin of kimberlite and diamond. Chemical Geology, 262(1-2), 29-41.

Litasov, K.D., Safonov, O.G., and Ohtani, E. (2010) Origin of Cl-bearing silica-rich melt inclusions in diamonds: Experimental evidence for an eclogite connection. Geology, 38(12), 1131-1134.

Navon, O., Hutcheon, I., Rossman, G., and Wasserburg, G. (1988) Mantle-derived fluids in diamond micro-inclusions. Nature, 335(6193), 784-789.

Newbury, D.E., and Ritchie, N.W.M. (2015) Performing elemental microanalysis with high accuracy and high precision by scanning electron microscopy/silicon drift detector energy-dispersive X-ray spectrometry (SEM/SDD-EDS). Journal of materials science, 50(2), 493-518.

Osugi, J., Shimizu, K., Inoue, K., and Yasunami, K. (1964) A compact cubic anvil high pressure apparatus. Review of Physical Chemistry of Japan, 34(1), 1-6.

Palme, H., and O'Neill, H.S.C. (2003) Cosmochemical estimates of mantle composition. In A.M. Davis, H.D. Holland, and K.K. Turekian, Eds. Treatise on geochemistry, 2, p. 1-38. Elsevier, New York.

Peh, E., Liedel, C., Taubert, A., and Tauer, K. (2017) Composition inversion to form calcium carbonate mixtures. CrystEngComm, 19(26), 3573-3583.

Pistorius, C.W.F.T. (1966) Effect of pressure on the melting points of the sodium halides. The Journal of Chemical Physics, 45(10), 3513-3519.

Rashchenko, S.V., Bakakin, V.V., Shatskiy, A.F., Gavryushkin, P.N., Seryotkin, Y.V., and Litasov, K.D. (2017) Noncentrosymmetric $Na_2Ca_4(CO_3)_5$ carbonate of "$M1_3M2_3XY_3Z$" structural type and affinity between borate and carbonate structures for design of new optical materials. Crystal Growth & Design, 17(11), 6079-6084.

Rashchenko, S.V., Shatskiy, A.F., Arefiev, A.V., Seryotkin, Y.V., and Litasov, K.D. (2018) $Na_4Ca(CO_3)_3$: a novel carbonate analog of borate optical materials. CrystEngComm, 20, 5228-5232.

Safonov, O.G., Perchuk, L.L., and Litvin, Y.A. (2007) Melting relations in the chloride-carbonate-silicate systems at high-pressure and the model for formation of alkalic diamond-forming liquids in the upper mantle. Earth and Planetary Science Letters, 253(1-2), 112-128.

Safonov, O.G., Chertkova, N.V., Perchuk, L.L., and Litvin, Y.A. (2009a) Experimental model for alkalic chloride-rich liquids in the upper mantle. Lithos, 112, 260-273.

Safonov, O.G., Perchuk, L.L., Yapaskurt, V.O., and Litvin, Y.A. (2009b) Immiscibility of carbonate-silicate and chloride-carbonate melts in the kimberlite-$CaCO_3$-Na_2CO_3-KCl system at 4.8 GPa. Doklady Earth Sciences, 424(3), 388-392.

Safonov, O.G., Kamenetsky, V.S., and Perchuk, L.L. (2011) Links between carbonatite and kimberlite melts in chloride–carbonate–silicate systems: experiments and application to natural assemblages. Journal of Petrology, 52(7-8), 1307-1331.

Schrauder, M., and Navon, O. (1994) Hydrous and carbonatitic mantle fluids in fibrous diamonds from Jwaneng, Botswana. Geochimica et Cosmochimica Acta, 58(2), 761-771.

Sharp, Z.D., Barnes, J.D., Brearley, A.J., Chaussidon, M., Fischer, T.P., and Kamenetsky, V.S. (2007) Chlorine isotope homogeneity of the mantle, crust and carbonaceous chondrites. Nature, 446(7139), 1062-1065.

Sharp, Z.D., and Draper, D.S. (2013) The chlorine abundance of Earth: implications for a habitable planet. Earth and Planetary Science Letters, 369, 71-77.

Sharygin, I.S., Golovin, A.V., Tarasov, A.A., Dymshits, A.M., and Kovaleva, E. (2021) Confocal Raman spectroscopic study of melt inclusions in olivine of mantle xenoliths from the Bultfontein kimberlite pipe (Kimberley cluster, South Africa): Evidence for

alkali-rich carbonate melt in the mantle beneath Kaapvaal Craton. Journal of Raman Spectroscopy, https://doi.org/10.1002/jrs.6198.

Shatskiy, A., Katsura, T., Litasov, K.D., Shcherbakova, A.V., Borzdov, Y.M., Yamazaki, D., Yoneda, A., Ohtani, E., and Ito, E. (2011) High pressure generation using scaled-up Kawai-cell. Physics of the Earth and Planetary Interiors, 189(1-2), 92-108.

Shatskiy, A., Gavryushkin, P.N., Sharygin, I.S., Litasov, K.D., Kupriyanov, I.N., Higo, Y., Borzdov, Y.M., Funakoshi, K., Palyanov, Y.N., and Ohtani, E. (2013a) Melting and subsolidus phase relations in the system Na_2CO_3-$MgCO_3$+-H_2O at 6 GPa and the stability of $Na_2Mg(CO_3)_2$ in the upper mantle. American Mineralogist, 98(11-12), 2172-2182.

Shatskiy, A., Sharygin, I.S., Gavryushkin, P.N., Litasov, K.D., Borzdov, Y.M., Shcherbakova, A.V., Higo, Y., Funakoshi, K.-i., Palyanov, Y.N., and Ohtani, E. (2013b) The system K_2CO_3-$MgCO_3$ at 6 GPa and 900-1450 ºC. American Mineralogist, 98(8-9), 1593-1603.

Shatskiy, A., Sharygin, I.S., Litasov, K.D., Borzdov, Y.M., Palyanov, Y.N., and Ohtani, E. (2013c) New experimental data on phase relations for the system Na_2CO_3-$CaCO_3$ at 6 GPa and 900-1400 ºC. American Mineralogist, 98(11-12), 2164-2171.

Shatskiy, A., Podborodnikov, I.V., Arefiev, A.V., Minin, D.A., Chanyshev, A.D., and Litasov, K.D. (2018) Revision of the $CaCO_3$–$MgCO_3$ phase diagram at 3 and 6 GPa. American Mineralogist, 103(3), 441-452.

Shatskiy, A., Arefiev, A.V., Podborodnikov, I.V., and Litasov, K.D. (2019) Origin of K-rich diamond-forming immiscible melts and CO_2 fluid via partial melting of carbonated pelites at a depth of 180-200 km. Gondwana Research, 75(11), 154-171.

Shatskiy, A., Bekhtenova, A., Arefiev, A.V., Podborodnikov, I.V., Vinogradova, Y.G., Rezvukhin, D.I., and Litasov, K.D. (2022) Solidus and melting of carbonated phlogopite peridotite at 3-6.5 GPa: Implications for mantle metasomatism. Gondwana Research, 101, 156-174.

435 Shatsky, V., Zedgenizov, D., Ragozin, A., and Kalinina, V. (2019) Silicate melt Inclusions in
436 diamonds of eclogite paragenesis from placers on the Northeastern Siberian craton.
437 Minerals, 9(7), 412.
438 Shimizu, K., Saal, A.E., Myers, C.E., Nagle, A.N., Hauri, E.H., Forsyth, D.W., Kamenetsky,
439 V.S., and Niu, Y. (2016) Two-component mantle melting-mixing model for the
440 generation of mid-ocean ridge basalts: implications for the volatile content of the Pacific
441 upper mantle. Geochimica et Cosmochimica Acta, 176, 44-80.
442 Veksler, I.V. (2004) Liquid immiscibility and its role at the magmatic–hydrothermal transition: a
443 summary of experimental studies. Chemical Geology, 210(1-4), 7-31.
444 Weiss, Y., McNeill, J., Pearson, D.G., Nowell, G.M., and Ottley, C.J. (2015) Highly saline fluids
445 from a subducting slab as the source for fluid-rich diamonds. Nature, 524(7565), 339-
446 342.
447 Zedgenizov, D.A., Ragozin, A.L., Shatsky, V.S., Araujo, D., Griffin, W.L., and Kagi, H. (2009)
448 Mg and Fe-rich carbonate-silicate high-density fluids in cuboid diamonds from the
449 Internationalnaya kimberlite pipe (Yakutia). Lithos, 112(S2), 638-647.
450 Zedgenizov, D.A., Ragozin, A.L., Shatsky, V.S., Araujo, D., and Griffin, W.L. (2011) Fibrous
451 diamonds from the placers of the northeastern Siberian Platform: carbonate and silicate
452 crystallization media. Russian Geology and Geophysics, 52(11), 1298-1309.
453 Zedgenizov, D.A., Ragozin, A.L., Shatsky, V.S., and Griffin, W.L. (2018) Diamond formation
454 during metasomatism of mantle eclogite by chloride-carbonate melt. Contributions to
455 Mineralogy and Petrology, 173(10), 84.

456

457

458 **Figure captions**

459

460 Figure 1. BSE images of selected sample cross-sections in the NaCl−$CaCO_3$ system at 6 GPa and
461 1100 °C (a-c), 1200 °C (d), 1250 °C (e-g), and pure NaCl at 1500 °C (h, i). HT – high-temperature
462 side. LT – low-temperature side. The gravity vector is directed downward.

463

464 Figure 2. Phase relations in the 2NaCl-$CaCO_3$ system at 6 GPa. Positions of large circles denote
465 bulk compositions of samples, whereas segments indicate phases present in the recovered samples.
466 Smaller grey circles indicate the composition of melt measured by EDS. The $CaCO_3$ melting point
467 is after (Shatskiy et al. 2018). The phase transitions in $CaCO_3$: aragonite, calcite-V (*R*-3*m*), and
468 calcite-Vb ($P2_1/m$) are after (Druzhbin et al. Under review).

469

470 Figure 3. BSE images of sample cross-sections in the system NaCl−$MgCO_3$ at 6 GPa and 1250 (a-
471 c), 1300 (d-f), 1400 °C (g, h), and 1500 °C (i). HT – high-temperature side. LT – low-temperature
472 side. The gravity vector is directed downward.

473

474 Figure 4. Phase relations in the 2NaCl-$MgCO_3$ system at 6 GPa. Positions of large circles denote
475 bulk compositions of samples, whereas segments indicate phases present in the recovered samples.
476 Smaller grey circles indicate the composition of melt measured by EDS. The $MgCO_3$ melting point
477 is after (Shatskiy et al. 2018).

478

479 Figure 5. BSE images of sample cross-sections in the NaCl−$CaCO_3$ system at 6 GPa and 1100 °C
480 under hydrous conditions. HT – high-temperature side. LT – low-temperature side. The gravity
481 vector is directed downward.

482

Figure 6. Phase relations in the 2NaCl-$CaCO_3$ system established at 6 GPa and 1100 °C in undried samples, presumably containing water (blue), compared with the phase relations established under nominally dry conditions (black). The phase transitions in $CaCO_3$ are after (Druzhbin et al. Under review). (Color online).

Figure 7. Comparison of phase relations in the systems NaCl–$CaCO_3$ (this study) (a), Na_2CO_3–$CaCO_3$ (Shatskiy et al. 2013c) (b), NaCl–$MgCO_3$ (this study) (c), and Na_2CO_3–$MgCO_3$ (Shatskiy et al. 2013a) (d) at 6 GPa. The phase transitions in $CaCO_3$ are after (Druzhbin et al. Under review).

Figure 8. Schematic diagrams illustrating the possible genetic link between saline and carbonatitic HDFs: via fraction crystallization of asthenosphere or plume-derived Cl-bearing carbonatitic melt (Shatskiy et al. 2019) (a); progressive melting of carbonated mantle domains involving slab-derived saline HDF (Weiss et al. 2015) (b); and reduction of the slab- or plume-derived Cl-bearing carbonatitic melt infiltrating reduced ambient mantle (c). (Color online)

Table 1. Run conditions and phase compositions (mol%) in the NaCl-$CaCO_3$ system at 6 GPa.

Run	*T*, °C	*t*, h	#	Na2#	Phases	n	Ca	2Na	2Cl	CO_3
D281	1000	98	3-2	18	Bulk	–	40.9	9.1	9.1	40.9
					Hl	7	0.2(2)	49.8(2)	50.0(7)	b.d.l.
					Arg	9	50.0(0)	b.d.l.	0.1(1)	49.9(1)
–//–			4-2	33	Bulk	–	33.3(0)	16.7(0)	16.7	33.3
					Hl	7	b.d.l.	50.0(0)	50.7(2)	b.d.l.
					Arg	9	50.0(0)	b.d.l.	0.1(1)	49.9(1)
–//–			3-1	79	Bulk	–	10.7	39.3	35.6	14.4
					Hl	5	b.d.l.	50.0(0)	50.8(5)	b.d.l.
					Arg	7	50.0(1)	0.0(1)	0.3(0)	49.7(0)
D283	1100	48	4-1	33	Bulk	–	33.3	16.7	16.7	33.3
					Hl	1	0.1	49.9	49.7	0.3
					Arg	5	50.0(0)	b.d.l.	0.1(0)	49.9(1)
D227	–//–	37	4-2	46	Bulk	–	26.9	23.1	23.1	26.9
					Hl	5	0.1(2)	49.9(2)	51.0(6)	b.d.l.
					Arg	5	50.0(0)	0.0(0)	0.1(1)	49.9(1)
D283	–//–	48	4-2	67	Bulk	–	16.7	33.3	33.3	16.7
					Hl	5	b.d.l.	50.0(0)	47.9(3.3)	2.1(3.3)
					Arg	5	50.0(0)	0.0(0)	0.2(1)	49.7(1)
D227	–//–	37	4-1	82	Bulk	–	8.8	41.2	41.2	8.8
					Hl	5	0.2(2)	49.8(2)	50.6(3)	b.d.l.
					Arg	7	49.9(1)	0.1(1)	0.4(0)	49.6(0)
D282	1200	24	4-1	36	Bulk	–	33.3	16.7	16.7	33.3
					L(37)	1	31.5	18.4	16.6	33.3
–//–			4-2	67	Bulk	–	16.7	33.3	33.3	16.7
					Hl	1	0.1	49.9	49.2	0.8
					L(41)	2	29.5	20.5	18.1	31.8
D265	1250	3	3-2	18	Bulk	–	40.9	9.1	9.1	40.9
					Arg	1	50.0	0.0	0.1	49.9
					L(33)	5	33.6(3)	16.4(3)	15.8(2)	34.2(2)
D266	–//–	7	3-2	18	Bulk	–	40.9	9.1	9.1	40.9
					Arg	1	50.0	0.0	0.0	50.0
					L(32)	5	33.8(2)	16.2(2)	15.4(1)	34.6(1)
–//–			3-1	82	Bulk	–	8.8	41.2	41.2	8.8
					Hl	6	0.2(1)	49.8(1)	50.2(9)	b.d.l.
					L(61)	5	19.5(4)	30.4(3)	27.8(3)	22.2(3)
D265	–//–	3	3-1	95	Bulk	–	2.6	47.4	47.4	2.6
					Hl	7	0.1(1)	49.9(1)	49.8(3)	0.2(3)
					L(59)	5	20.0(4)	29.4(5)	25.2(1.2)	24.7(1.2)
D216	1300	4	3-3	33	Bulk	–	33.3	16.7	16.7	33.3
					L(33)	1	33.3	16.7	16.7	33.3
D284	–//–	3	3-1	92	Bulk	–	4.1	45.9	45.9	4.1
					Hl	8	0.1(1)	49.9(1)	49.1(2)	0.9(2)
					L(68)	5	15.9(3)	34.1(3)	29.8(3)	20.2(3)
D263	1400	2	3-1	40	Bulk	–	29.9	20.1	18.5	31.5
					L(40)	5	29.9(0)	20.1(0)	18.7(2)	31.3(2)
–//–			3-2	95	Bulk	–	2.6	47.4	47.4	2.6
					Hl	5	0.1(2)	49.9(2)	51.2(4)	b.d.l.
					L(91)	5	4.3(2)	45.7(2)	47.2(3)	2.8(3)
D287	1500	1	3-2	6	Bulk	–	47.1	2.9	2.9	47.1
					L(3)	5	48.5(2)	1.5(2)	1.8(0)	48.1(1)
D223	–//–	6	4-2	46	Bulk	–	26.9	23.1	23.1	26.9
					L(43)	1	28.7	21.3	19.6	30.4
–//–			4-1	82	Bulk	–	8.8	41.2	41.2	8.8
					L(75)	1	12.4	37.6	37.4	12.6
D287	–//–	6	3-3	100	Bulk	–	0	50.0	50.0	0
					Hl	1	0.0	50.0	49.3	0.7
					L(100)	1	0.0	49.9	49.2	0.6
D224	1600	3	4-2	32	L(32)	1	34.3	15.9	15.4	34.4
			4-1	82	L982)	1	9.2	40.6	40.3	9.3

Notes: *t* – run duration; Na2# = 100·2NaCl/(2NaCl+$CaCO_3$) reflects the molar fraction of halite in the starting compositions; L(32) – liquid with Na2# 32, n – number of SDD-EDS analysis; standard deviations are given in brackets.

Table 2. Run conditions and phase compositions (mol%) in the NaCl-$MgCO_3$ system at 6 GPa.

Run	*T*, °C	*t*, h	#	Na2#	Phases	n	Mg	2Na	2Cl	CO_3
D227	1100	37	3-1	46	Bulk	−	26.9	23.1	23.1	26.9
					Hl	5	b.d.l.	50.0(0)	51.1(5)	b.d.l.
					Mgs	5	49.8(0)	b.d.l.	0.1(0)	49.9(0)
−//−			3-3	82	Bulk	−	8.8	41.2	41.2	8.8
					Hl	5	b.d.l.	50.0(0)	50.9(3)	b.d.l.
					Mgs	5	49.8(2)	b.d.l.	0.1(1)	49.9(1)
D218	1200	18	3-4	46	Bulk	−	26.9	23.1	23.1	26.9
					Hl	1	b.d.l.	50.0	51.3	b.d.l.
					Mgs	2	49.9	0.0	0.1	49.9
−//−			3-3	82	Bulk	−	8.8	41.2	41.2	8.8
					Hl	5	b.d.l.	50.0(0)	50.2(2)	b.d.l.
					Mgs	5	49.7(1)	0.1(0)	0.1(0)	49.9(0)
D265	1250	3	3-4	18	Bulk	−	40.9	9.1	9.1	40.9
					Hl	5	b.d.l.	50.0(0)	49.8(5)	0.2(5)
					Mgs	5	49.8(0)	b.d.l.	b.d.l.	50.0(0)
D266	−//−	7	4-2	18	Bulk	−	40.9	9.1	9.1	40.9
					Hl	5	b.d.l.	50.0(0)	50.7(5)	b.d.l.
					Mgs	5	49.8(0)	b.d.l.	b.d.l.	50.0(0)
−//−			4-1	82	Bulk	−	8.8	41.2	41.2	8.8
					Hl	5	b.d.l.	50.0(0)	50.3(8)	b.d.l.
					Mgs	5	49.8(0)	b.d.l.	0.1(0)	49.9(0)
D265	−//−	3	3-4	95	Bulk	−	2.6	47.4	47.4	2.6
					Hl	9	b.d.l.	50.0(0)	49.4(3)	0.6(3)
					Mgs	6	49.8(0)	b.d.l.	0.1(0)	49.9(0)
D284	1300	3	3-2	18	Bulk	−	40.9	9.1	9.1	40.9
					Hl	1	b.d.l.	50.0	49.1	0.9
					Mgs	3	49.9	0.1	b.d.l.	49.8
					L(63)	3	18.4	31.2	32.4	18.0
D216	−//−	4	3-4	46	Bulk	−	26.9	23.1	23.1	26.9
					Hl	2	0.3	49.7	49.0	1.0
					Mgs	2	50.0	b.d.l.	b.d.l.	50.0
					L(64)	1	18.0	31.4	30.7	19.3
−//−			3-3	82	Bulk	−	8.8	41.2	41.2	8.8
					Hl	1	b.d.l.	50.0	49.1	0.9
					Mgs	1	49.9	0.1	0.1	49.9
					L(64)	1	17.9	31.9	30.2	19.8
D284	−//−	4	4-2	86	Bulk	−	7.1	42.9	42.9	7.1
					Hl	1	b.d.l.	50.0	49.5	0.3
					Mgs	1	49.7	0.1	0.1	49.9
					L(64)	3	16.7	30.3	27.9	25.1
D286	1400	2	3-2	46	Bulk	−	26.9	23.1	23.1	26.9
					Mgs	5	50.0(0)	b.d.l.	b.d.l.	50.0(0)
					L(58)	5	21.2(3)	28.9(3)	28.9(3)	21.1(4)
D220	−//−	4	3-1	73	Bulk	−	13.6	36.4	36.6	13.4
					L(72)	5	13.7(2)	36.2(2)	36.6(1)	13.4(1)
D286	−//−	2	3-1	97	Bulk	−	1.3	48.7	48.7	1.3
					Hl	5	b.d.l.	50.0(2)	49.5(4)	0.5(4)
					L(78)	5	10.8(4)	39.1(4)	38.5(5)	11.5(5)
D287	1500	1	4-2	33	Bulk	−	33.3	16.7	16.7	33.3
					Mgs	1	50.0	0.0	0.0	50.0
					L(44)	1	27.7	21.3	19.7	31.3
D223	−//−	6	3-4	46	Bulk	−	26.9	23.1	23.1	26.9
					L(44)	1	27.8	22.2	20.4	29.6
−//−					Bulk	−	8.8	41.2	41.2	8.8
					L(79)	1	10.5	39.5	39.6	10.4
D224	1600	3	3-4	38	L(38)	1	30.7	19.2	18.3	31.7
			3-3	79	L(79)	1	10.3	39.6	41.2	8.8

Notes: *t* – run duration; Na2# = 100·2NaCl/(2NaCl+$MgCO_3$) reflects the molar fraction of halite in the starting compositions; L(46) – liquid with Na2# 46, n – number of SDD-EDS analysis; standard deviations are given in brackets.

Fig. 1

Run No.; Na2#, mol%; temperature; run duration.

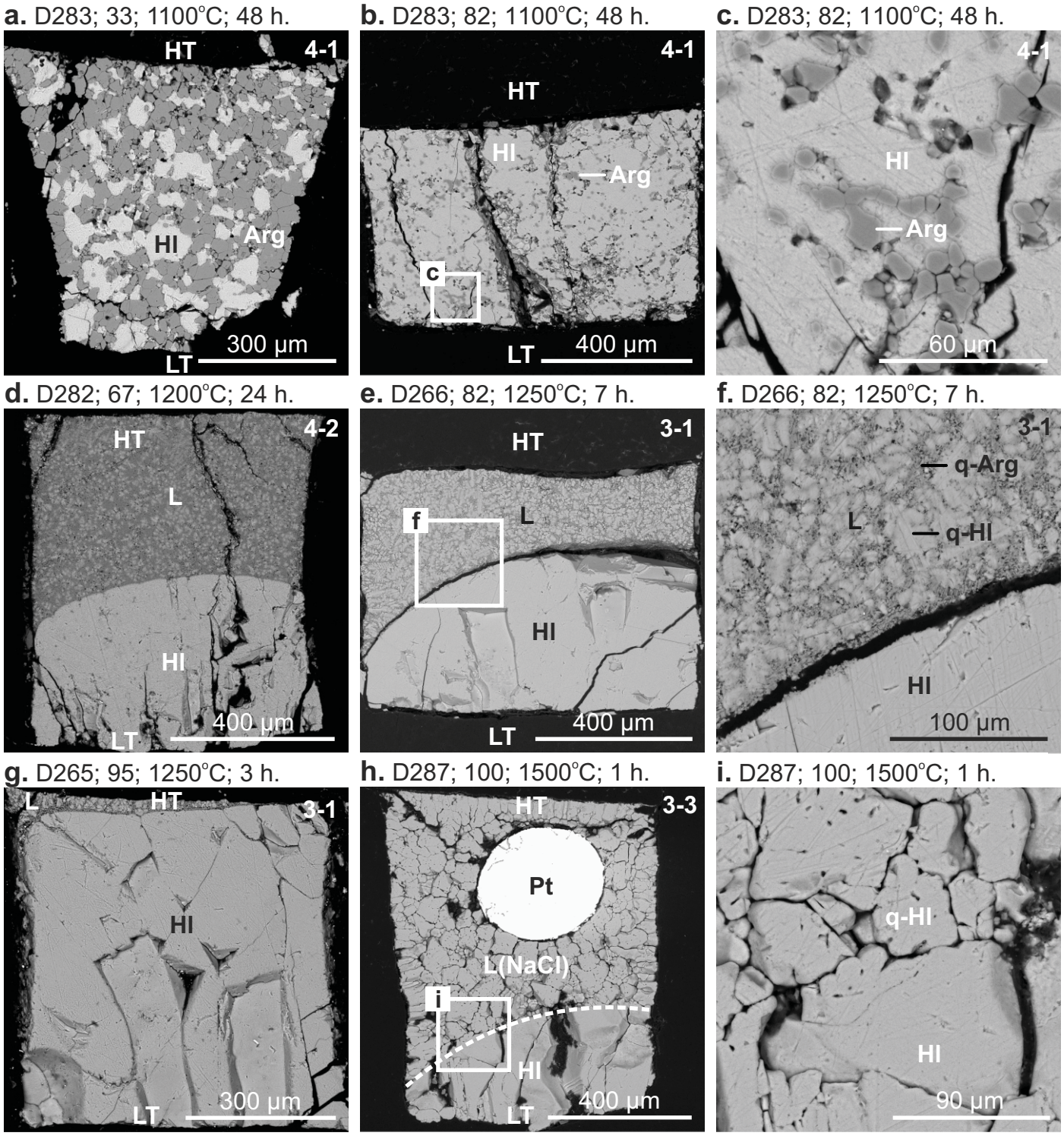

Fig. 2

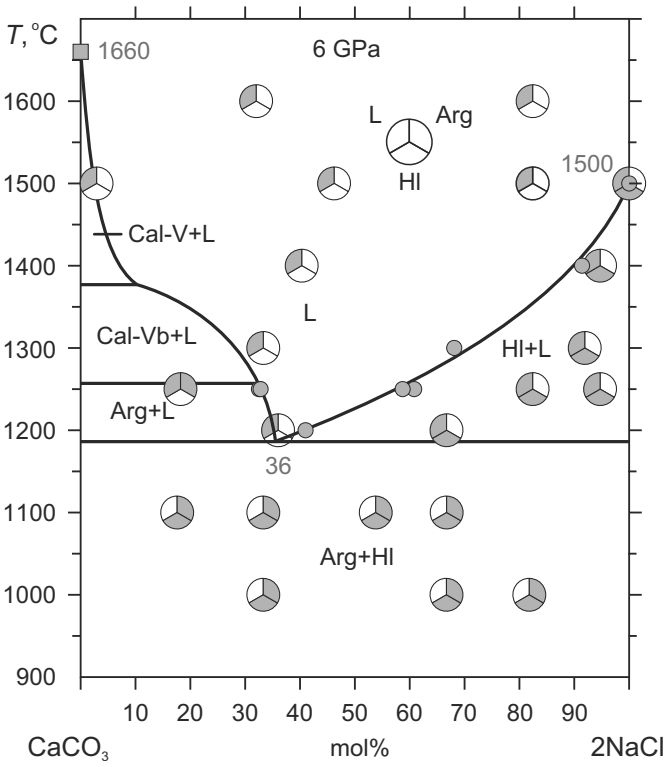
T, °C
1660
6 GPa
1600
L
Arg
Hl
1500
1500
Cal-V+L
1400
L
Cal-Vb+L
1300
Hl+L
Arg+L
1200
36
1100
Arg+Hl
1000
900
10 20 30 40 50 60 70 80 90
CaCO3
mol%
2NaCl

Fig. 3

Run No.; Na2#, mol%; temperature; run duration.

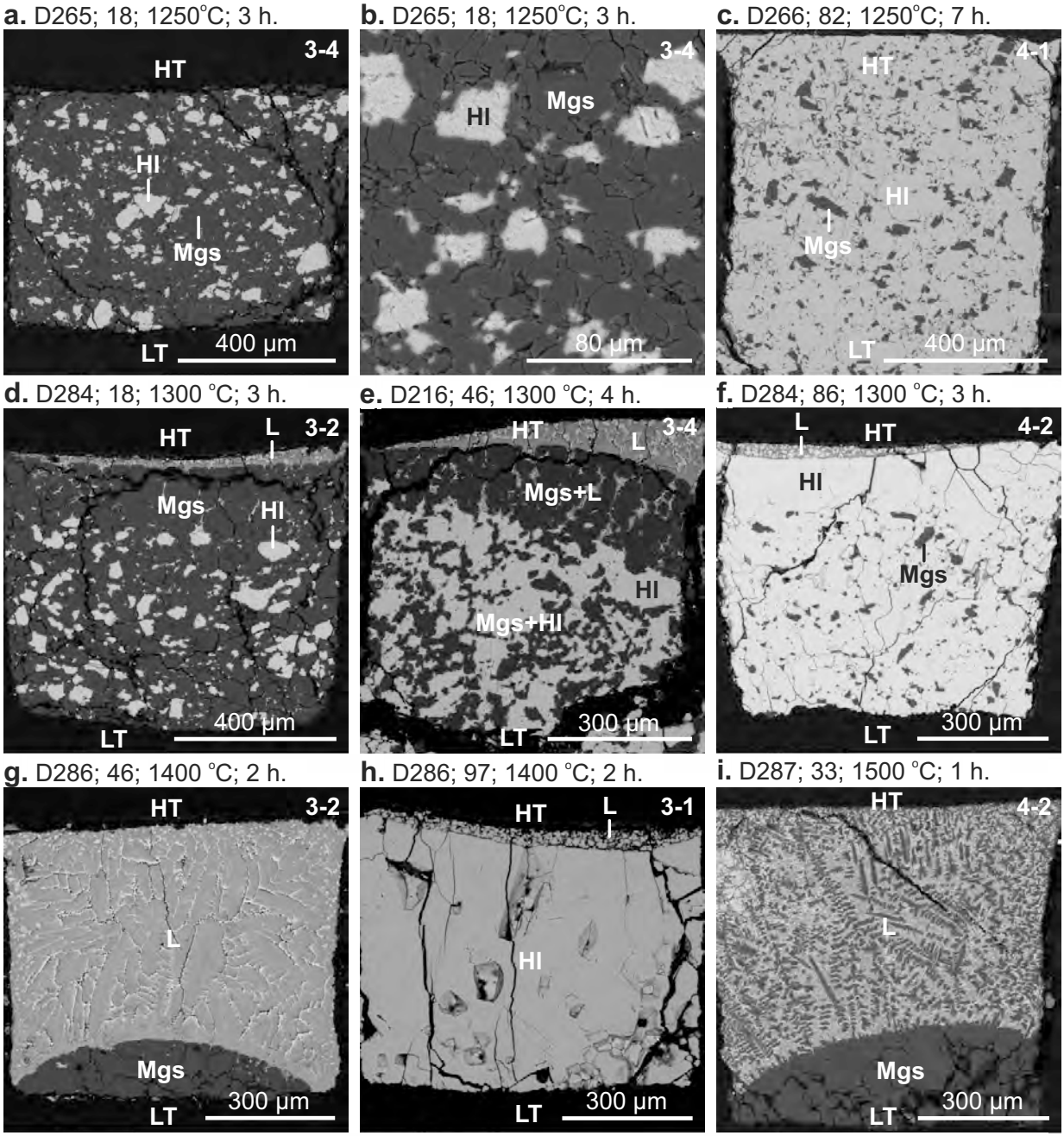

Fig. 4

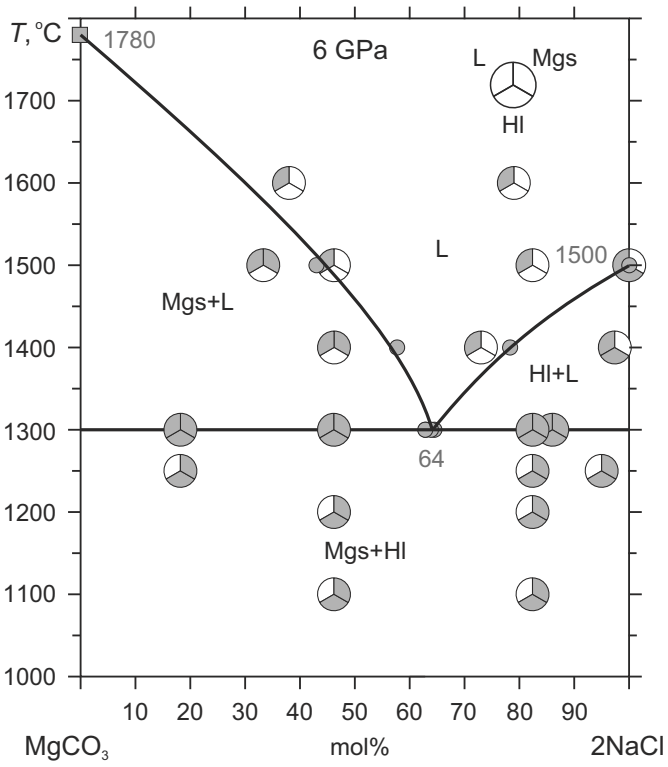
T, °C
1780
6 GPa
L
Mgs
Hl
1700
1600
1500
1400
1300
1200
1100
1000
L
1500
Mgs+L
Hl+L
64
Mgs+Hl
10
20
30
40
50
60
70
80
90
MgCO3
mol%
2NaCl

Fig. 5

Run No.; Na2#, mol%; temperature; run duration.

a. D271; 18; 1100°C; 5 h. **b.** D271; 67; 1100°C; 5 h. **c.** D271; 82; 1100°C; 5 h.

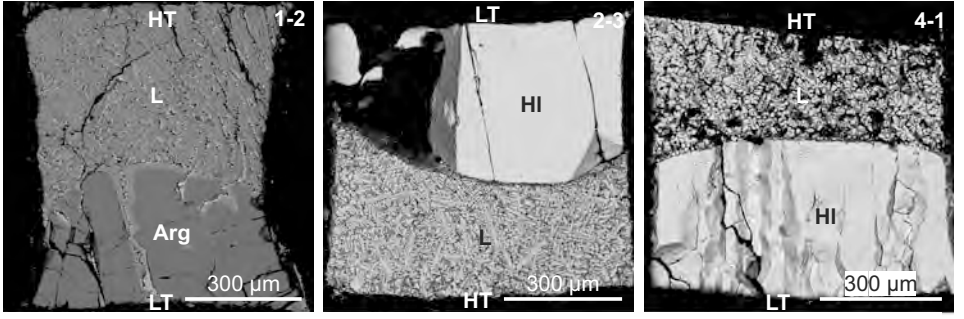

Fig. 6

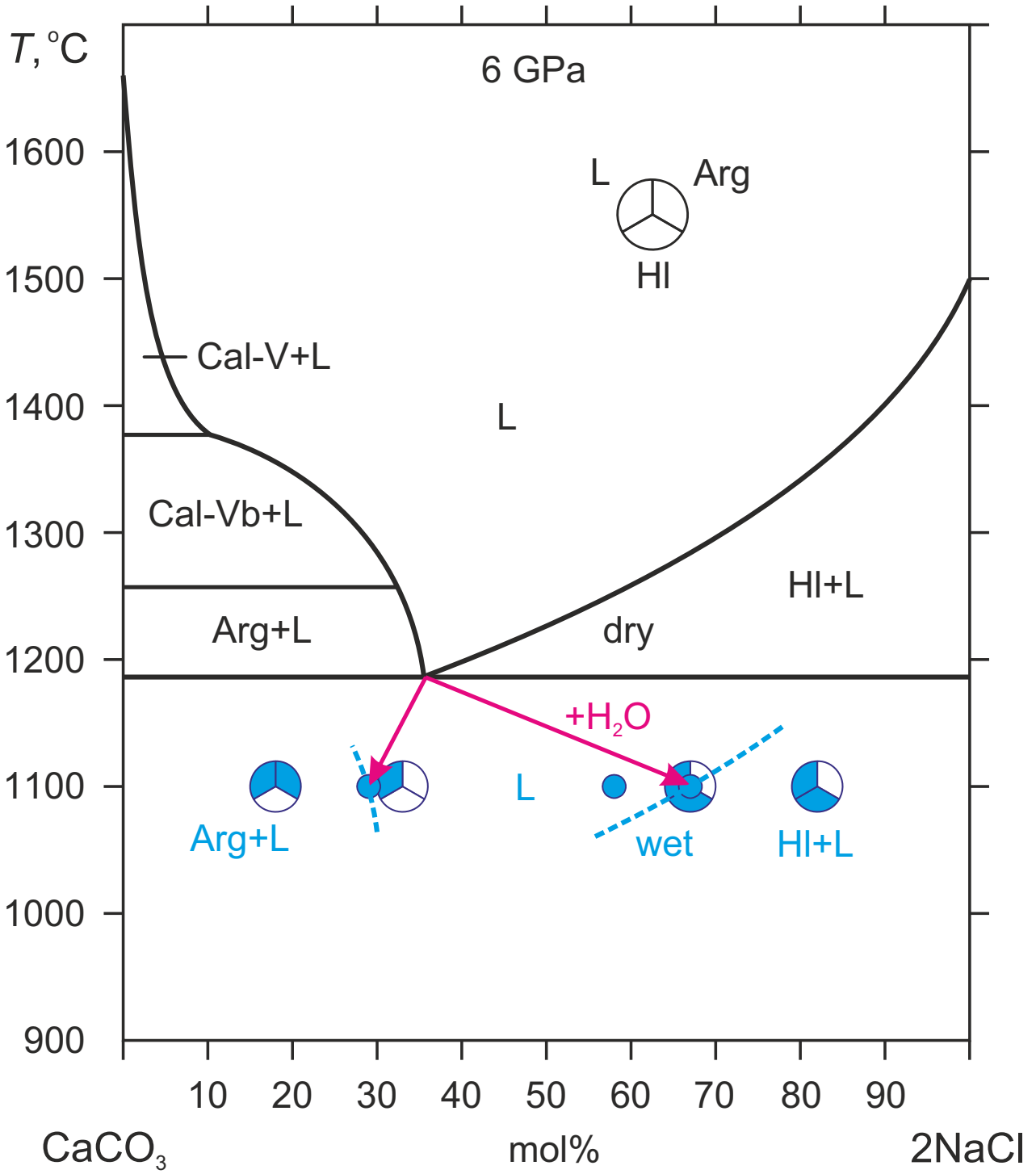
T, °C
6 GPa
1600
1500
1400
1300
1200
1100
1000
900
L
Arg
Hl
Cal-V+L
L
Cal-Vb+L
Hl+L
Arg+L
dry
+H2O
Arg+L
L
wet
Hl+L
10
20
30
40
50
60
70
80
90
CaCO3
mol%
2NaCl

Fig. 7

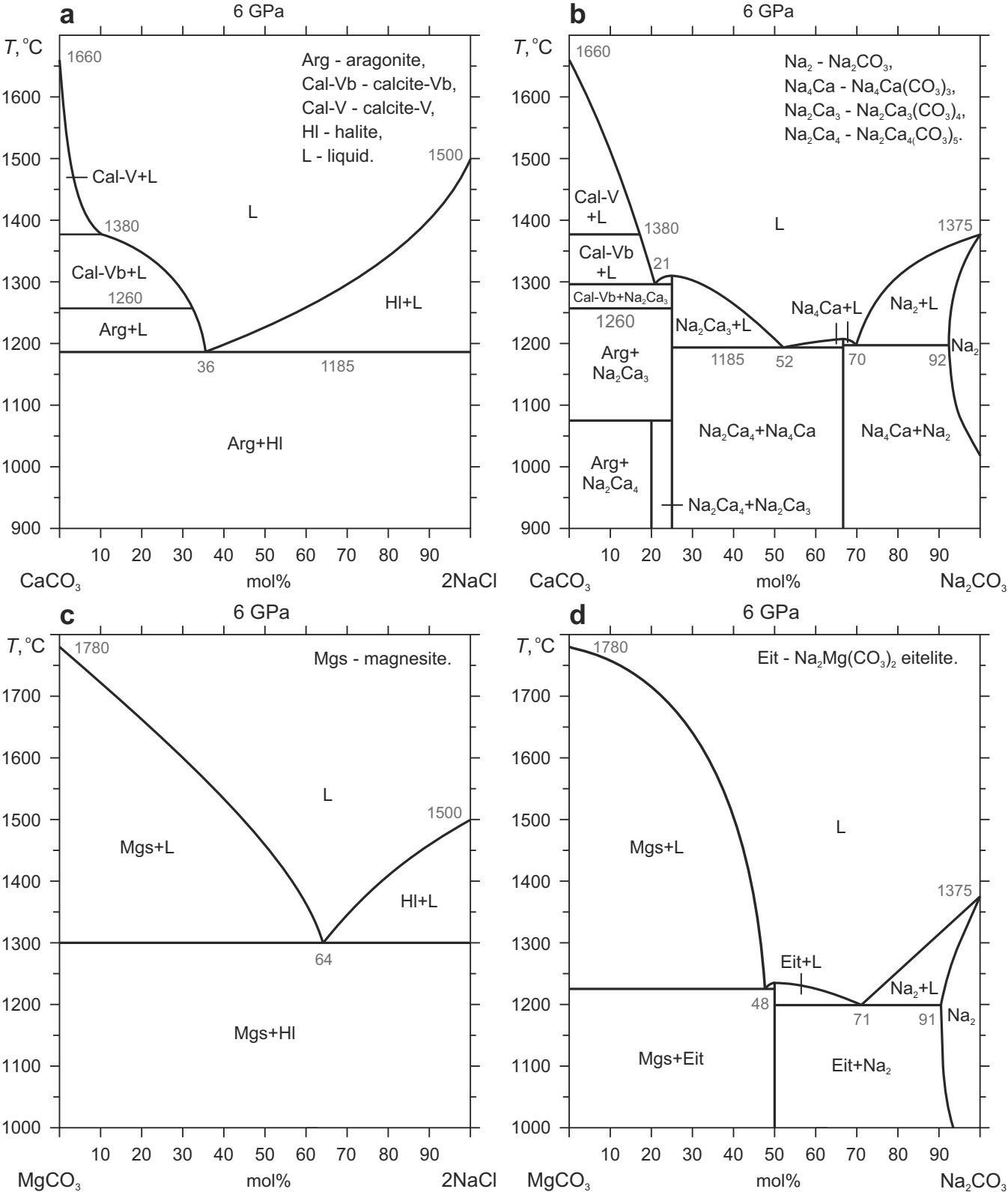
a
6 GPa
T, °C
1660
Arg - aragonite,
Cal-Vb - calcite-Vb,
Cal-V - calcite-V,
Hl - halite,
L - liquid.
1500
Cal-V+L
L
1380
Cal-Vb+L
1260
Hl+L
Arg+L
36
1185
Arg+Hl
CaCO3
mol%
2NaCl
b
6 GPa
T, °C
1660
Na2 - Na2CO3,
Na4Ca - Na4Ca(CO3)3,
Na2Ca3 - Na2Ca3(CO3)4,
Na2Ca4 - Na2Ca4(CO3)5.
Cal-V +L
1380
L
1375
Cal-Vb +L
21
Cal-Vb+Na2Ca3
1260
Na2Ca3+L
Na4Ca+L
Na2+L
Arg+ Na2Ca3
1185
52
70
92
Na2
Na2Ca4+Na4Ca
Na4Ca+Na2
Arg+ Na2Ca4
Na2Ca4+Na2Ca3
CaCO3
mol%
Na2CO3
c
6 GPa
T, °C
1780
Mgs - magnesite.
L
1500
Mgs+L
Hl+L
64
Mgs+Hl
MgCO3
mol%
2NaCl
d
6 GPa
T, °C
1780
Eit - Na2Mg(CO3)2 eitelite.
L
Mgs+L
1375
Eit+L
Na2+L
48
71
91
Na2
Mgs+Eit
Eit+Na2
MgCO3
mol%
Na2CO3

Fig. 8

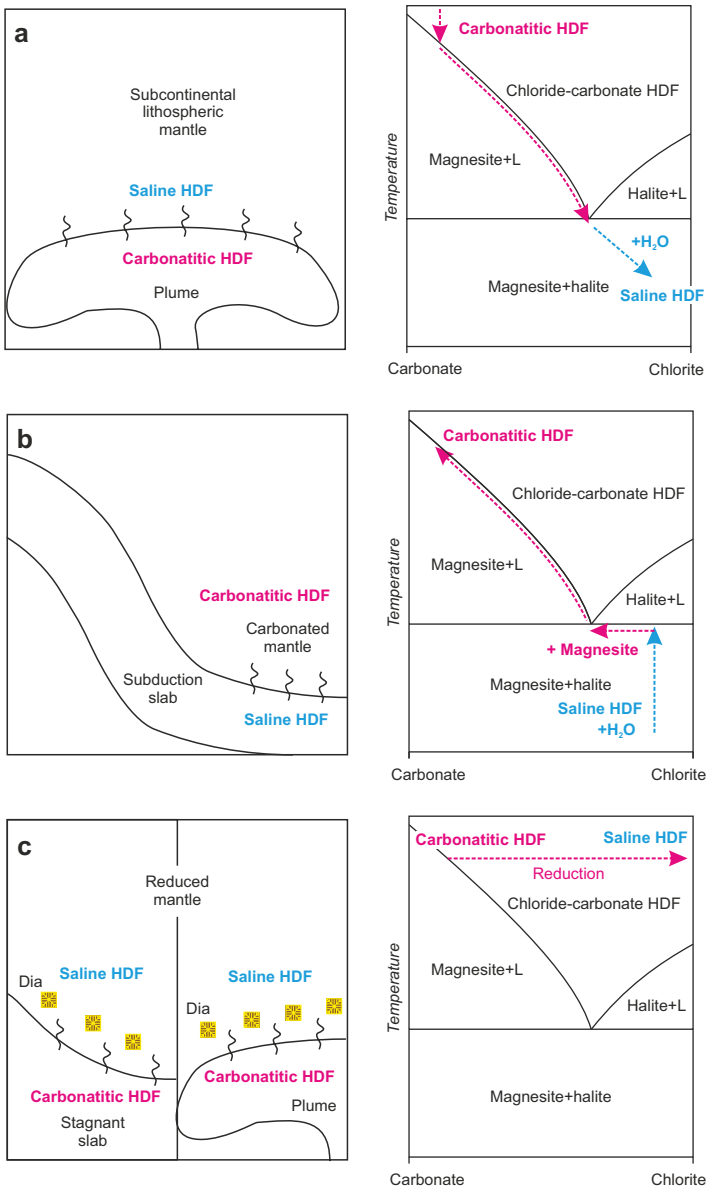
a
Subcontinental lithospheric mantle
Saline HDF
Carbonatitic HDF
Plume
Carbonatitic HDF
Chloride-carbonate HDF
Magnesite+L
Halite+L
Temperature
+H2O
Magnesite+halite
Saline HDF
Carbonate
Chlorite
b
Carbonatitic HDF
Carbonated mantle
Subduction slab
Saline HDF
Carbonatitic HDF
Chloride-carbonate HDF
Magnesite+L
Halite+L
Temperature
+ Magnesite
Magnesite+halite
Saline HDF
+H2O
Carbonate
Chlorite
c
Reduced mantle
Dia
Saline HDF
Saline HDF
Dia
Carbonatitic HDF
Carbonatitic HDF
Plume
Stagnant slab
Carbonatitic HDF
Saline HDF
Reduction
Chloride-carbonate HDF
Magnesite+L
Halite+L
Temperature
Magnesite+halite
Carbonate
Chlorite